

## Article

# Hybrid Nanostructures of Fe<sub>3</sub>O<sub>4</sub> and Au Prepared via Coprecipitation and Ultrasonic Spray Pyrolysis

Lan Kresnik <sup>1</sup>, Peter Majerič <sup>1,2</sup> , Darja Feizpour <sup>3</sup> , Klementina Pušnik Črešnar <sup>1,4</sup> and Rebeka Rudolf <sup>1,2,5,\*</sup> 

<sup>1</sup> Faculty of Mechanical Engineering, University of Maribor, 2000 Maribor, Slovenia; lan.kresnik1@um.si (L.K.); peter.majeric@um.si (P.M.); klementina.pusnik@um.si (K.P.Č.)

<sup>2</sup> Zlatarna Celje d.o.o., 3000 Celje, Slovenia

<sup>3</sup> Institute of Metals and Technology (IMT), 1000 Ljubljana, Slovenia; darja.feizpour@imt.si

<sup>4</sup> Faculty of Chemistry and Chemical Engineering, University of Maribor, 2000 Maribor, Slovenia

<sup>5</sup> Pomurje Science and Innovation Centre, 9000 Murska Sobota, Slovenia

\* Correspondence: rebeka.rudolf@um.si

**Abstract:** The coupled processes of coprecipitation and ultrasonic spray pyrolysis (USP) were used to synthesize Fe<sub>3</sub>O<sub>4</sub>-Au hybrid nanostructures. The first coprecipitation method enabled the synthesis of Fe<sub>3</sub>O<sub>4</sub> nanoparticles by mixing iron salts' ions (Fe<sup>2+</sup> and Fe<sup>3+</sup>) and ammonia as the base, and USP was used as the coating process of the Fe<sub>3</sub>O<sub>4</sub> nanoparticles with Au. The formatted hybrid nanostructures consist of Fe<sub>3</sub>O<sub>4</sub> nanoparticles that have Au on their surface in the form of gold nanoparticles (AuNPs). AuNPs have a crystalline structure and range in size from 10 to 200 nm. Additional characterization techniques, including ICP-OES, TEM, SEM, EDS, DLS, zeta potential, and room temperature magnetic hysteresis loops, were used to determine the chemical, physical, and magnetic properties of the Fe<sub>3</sub>O<sub>4</sub> nanoparticles and hybrid nanostructures. It was found that USP produces separate AuNPs too (not just on the Fe<sub>3</sub>O<sub>4</sub> surface), suggesting a bimodal formation of AuNPs. The zeta potential of the Fe<sub>3</sub>O<sub>4</sub> nanoparticles showed poor stability (−15 mV), indicating a high tendency to aggregate, and the zeta potential of the hybrid nanostructures was also very low (≅0), which, comparatively means even worse stability. The saturation magnetization of the Fe<sub>3</sub>O<sub>4</sub> nanoparticles was 35 emu/g, which is relatively lower than that of bulk Fe<sub>3</sub>O<sub>4</sub>, while the saturation magnetization of the hybrid nanostructures was significantly lower (0.1 emu/g) compared to the Fe<sub>3</sub>O<sub>4</sub> nanoparticles.

**Keywords:** magnetic NPs; gold NPs; transmission electron microscopy; magnetic properties



**Citation:** Kresnik, L.; Majerič, P.; Feizpour, D.; Črešnar, K.P.; Rudolf, R. Hybrid Nanostructures of Fe<sub>3</sub>O<sub>4</sub> and Au Prepared via Coprecipitation and Ultrasonic Spray Pyrolysis. *Metals* **2024**, *14*, 1324. <https://doi.org/10.3390/met14121324>

Academic Editors: Jiro Kitagawa and Cristian Ciobanu

Received: 26 September 2024

Revised: 20 November 2024

Accepted: 21 November 2024

Published: 23 November 2024



**Copyright:** © 2024 by the authors. Licensee MDPI, Basel, Switzerland. This article is an open access article distributed under the terms and conditions of the Creative Commons Attribution (CC BY) license (<https://creativecommons.org/licenses/by/4.0/>).

## 1. Introduction

Nanoparticles (NPs) are materials with dimensions in the nanometer range, typically between 1 and 100 nanometers. At this scale, unique magnetic properties emerge, distinguishing them from their bulk counterparts. Fe<sub>3</sub>O<sub>4</sub> represents a special class of magnetic NPs that can interact with an external magnetic field as a direct consequence of their superparamagnetic, ferrimagnetic, and/or ferromagnetic properties [1]. Fe<sub>3</sub>O<sub>4</sub> has gained great attention in the past decade because of its promising results in various fields [2]. Fe<sub>3</sub>O<sub>4</sub> NPs have become a crucial tool in the biomedical area, significantly transforming different diagnostic and therapeutic methods. Due to their distinctive magnetic properties, as well as their compatibility with biological systems, and capacity to be modified on the surface, these materials are highly suitable for a wide range of applications, including magnetic resonance imaging (MRI) [3], targeted drug administration [4], and cancer therapy [5]. The potential of Fe<sub>3</sub>O<sub>4</sub> in biomedical applications is extensive, and current research is investigating novel and effective methods to employ these NPs. The prospects involve the advancement of multifunctional Fe<sub>3</sub>O<sub>4</sub>, with the ability to perform both diagnosis and treatment simultaneously, commonly known as ‘theragnostic’ [6–8]. Fe<sub>3</sub>O<sub>4</sub> NPs have a

significant benefit in their large surface area-to-volume ratio, enabling various functionalization and alterations that respond to specific biomedical requirements. The ability to adapt allows for the creation of magnetite ( $\text{Fe}_3\text{O}_4$ ) with tailored characteristics [9].  $\text{Fe}_3\text{O}_4$ -based sensors have shown remarkable application in different fields, including food technology, lab testing, clinical diagnosis, and environmental monitoring [10].  $\text{Fe}_3\text{O}_4$ -based biosensors have achieved tremendous status, due to distinct properties such as magnetic signaling and magnetic separation [11].

Despite the enormous potential of  $\text{Fe}_3\text{O}_4$  NPs, these materials are not ideal as active elements in sensing applications, which is why they have been used most often as capture/preconcentration elements in a sensing system, rather than as the sensor itself. This is because the low electrical conductivity and limited optical properties compromise the ability of  $\text{Fe}_3\text{O}_4$  to be the transducing element of a sensor [12]. Another challenge facing the use of  $\text{Fe}_3\text{O}_4$  in sensing is its large surface area-to-volume ratio and low surface charge at neutral pH, which typically results in low stability, with the  $\text{Fe}_3\text{O}_4$  tending to aggregate when dispersed in solvents [13]. Such aggregation can be reduced with appropriate surface chemistry, which is also vital for sensing applications [14]. However, the surfaces of most magnetic materials are not highly compatible with well-defined surface chemistry such as the alkanethiol system. Gold coating of the  $\text{Fe}_3\text{O}_4$  NPs addresses all the above-mentioned challenges, including conductivity, optical properties [15], biocompatibility [16], bioaffinity through functionalization of the amine/thiol terminal groups [17], and chemical stability by protecting the magnetic core from aggregation, oxidation, and corrosion [18].

Gold-coated  $\text{Fe}_3\text{O}_4$  NPs have been recognized and applied in analytical chemistry, mostly for bio-separation and the development of electrochemical and optical sensors [19]. Applications of these NPs in biomedicine have also been explored, including magnetic resonance imaging contrast agents [20], targeted drug delivery [21], as well as downstream processing [22]. The reason lies in their high versatility; the optical and magnetic properties of the NPs can be tuned and tailored to applications by changing their size, gold shell thickness, shape, charge, and surface modification [16].

More than two decades have passed since the first reports on the synthesis of gold-coated  $\text{Fe}_3\text{O}_4$  NPs, but challenges remain in different aspects of working with this category of NPs [23]. The first challenge is how to prepare highly monodisperse iron or iron oxide nanocrystals efficiently. This requires the NPs to be made with precise control of particle size and magnetic properties. The greater challenge is how to coat the core effectively with a smooth, complete, and tunable gold shell. The most common methods are to coat magnetic NPs by depositing gold directly onto the core surface or by using a chelating material between the core and the gold shell [16]. The properties of gold-coated  $\text{Fe}_3\text{O}_4$  NPs make overcoming these challenges worthwhile, and the last few years have seen considerable progress in their synthesis and application.

The aim of this research focuses on the synthesis of  $\text{Fe}_3\text{O}_4$  NPs using the coprecipitation method, followed by the formation of the Au coating using ultrasonic spray pyrolysis (USP). Different types of characterization techniques were used to confirm the hypothesis that an Au coating was reached on the resulting  $\text{Fe}_3\text{O}_4$  NPs, and to determine the properties of such a hybrid nanostructure.

## 2. Materials and Methods

### 2.1. $\text{Fe}_3\text{O}_4$ Synthesis with Coprecipitation

A total of 3.75 g of iron (II) sulfate heptahydrate (Sigma-Aldrich, Darmstadt, Germany) and 2.97 g of iron (III) sulfate hydrate (Sigma-Aldrich) were weighed into a 1000 mL beaker. A total of 500 mL of distilled water was added to the beaker, and the sulfates were allowed to dissolve. A solution of ammonia in water was prepared—3 mL of ammonia (Sigma-Aldrich) dissolved in 150 mL of distilled water. A pH meter was placed in the beaker. The ammonia solution was added dropwise to the beaker to raise the pH to 3. This pH was maintained for 30 min. Then, 250 mL of pure ammonia was added and left to stir for 30 min. A magnet was placed at the bottom of the beaker and the NPs were allowed

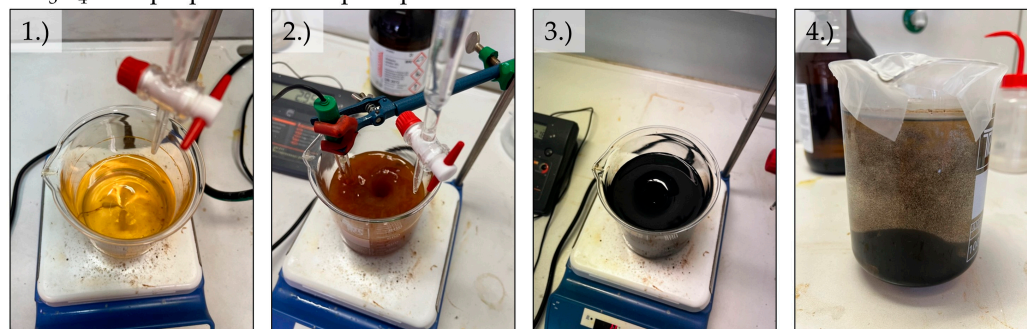
to settle. The remaining liquid was poured off, the magnet removed, and the NPs rinsed with distilled water. This was repeated 5 times. After examining the NPs using scanning electron microscopy, the decision was made to synthesize NPs using lower concentrations of both iron sulfates. Thus, three other syntheses were made, using 1/2, 1/4, and 1/8 of the original mass of iron sulfates. We determined that the suspension made with 0.47 g of iron (II) sulfate heptahydrate and 0.37 g of iron (III) sulfate hydrate (1/8) is the most appropriate for further characterization—the suspension appeared to have the least amount of aggregation of  $\text{Fe}_3\text{O}_4$ .

## 2.2. $\text{Fe}_3\text{O}_4$ Coating of Au with USP

For the experimental work, a proprietary USP device was used (Zlatarna Celje d.o.o., Celje, Slovenia), with an ultrasonic membrane with 1.65 MHz, a tube furnace with a quartz tube with a 1.5 m length and 35 mm internal diameter. The tube is separated into two heating zones with lengths of 0.5 and 1.0 m, for droplet evaporation and particle reaction, respectively. A reaction gas inlet is attached to the tube between these heating zones. The final particles are collected in 3 serially connected gas washing bottles, with a collection medium for stabilization.

The precursor solutions for USP were prepared by adding the suspension of  $\text{Fe}_3\text{O}_4$  obtained by the coprecipitation method (80 mL, containing 390 mg of  $\text{Fe}_3\text{O}_4$ ) to 700 mL of deionized (DI) water, and then adding 3.12 g of  $\text{AuCl}$  ( $\approx 50\%$  Au basis) (Glentham Life Sciences Ltd., Corsham, UK). The concentrations of  $\text{Fe}_3\text{O}_4$  and Au in the precursor solutions were 0.5 and 2 g/L, respectively. The evaporation zone was set at 200 °C, while the reaction zone was set at 400 °C. The carrier gas used was  $\text{N}_2$ , with a flow rate of 4 L/min, and the reduction gas used was  $\text{H}_2$  with a flow rate of 4 L/min. The synthesis was carried out for 2 h. The gas washing bottles contained 1.0 L of a water solution with an added 4.5 g/L of Polyvinylpyrrolidone (PVP) MW 30,000 (Sigma-Aldrich, Darmstadt, Germany) for the stabilization process. Figure 1 represents the preparation of our samples.

### $\text{Fe}_3\text{O}_4$ NPs preparation – coprecipitation method



### $\text{Fe}_3\text{O}_4$ -Au preparation – ultrasonic spray pyrolysis (USP)



**Figure 1.** (1.) Iron sulfates dissolving in distilled water; (2.) Raising the pH to 3; (3.) Addition of 250 mL of ammonia; (4.) NPs' settling; (5.) USP precursor solution; (6.) USP device; (7.) Final product  $\text{Fe}_3\text{O}_4$ -Au hybrid nanostructures.

### 2.3. X-Ray Diffraction (XRD)

The (XRD) measurements were conducted on a D8 Advance diffractometer (Bruker, Hamburg, Germany) equipped with Ni-filtered Cu-K $\alpha$  radiation (Bruker, Germany) at a scan rate of 0.24° per minute. XRD patterns were obtained over a range of 10 to 60 degrees (2 $\theta$ ).

### 2.4. Optical Emission Spectrometry with Inductively Coupled Plasma (ICP-OES)

An ICP-OES analysis was used for the determination of the elements in the Fe<sub>3</sub>O<sub>4</sub> and Fe<sub>3</sub>O<sub>4</sub>-Au hybrid nanostructures' suspensions. An HP, Agilent 7500 CE spectrometer, equipped with a collision cell (Santa Clara, CA, USA), was used to determine the Fe and Au content in the suspensions, with a power of 1.5 kW, a Meinhard nebulizer, a plasma gas flow of 15 L/min, a nebulizer gas flow of 0.85 L/min, a make-up gas flow of 0.28 L/min, and a reaction gas flow of 4.0 mL/min. The instrument was calibrated with matrix-matched calibration solutions, with a relative measurement uncertainty estimated as  $\pm 3\%$ .

### 2.5. Transmission Electron Microscopy (TEM) and Energy Dispersive X-Ray Spectroscopy (EDS)

The Fe<sub>3</sub>O<sub>4</sub> and Fe<sub>3</sub>O<sub>4</sub>-Au samples were characterized using scanning/transmission electron microscopy (S/TEM). A Talos F200i (Thermo Fisher Scientific, Waltham, MA, USA) TEM/STEM, operated at 200 kV, was employed for imaging, with an integrated Fast Fourier Transform (FFT) analysis to study the diffraction patterns, since X-ray Diffraction (XRD) analyses of the samples could not be performed because the samples were in solution and their amount was small. The application of FFT was critical for enhancing the clarity and analysis of diffraction patterns obtained from the TEM images. FFT allows for the transformation of spatial domain images into the frequency domain, highlighting periodic structures and crystallographic features that may not be readily apparent due to noise in the direct images. This analysis aids in the precise indexing of diffraction spots, and the determination of the NPs' crystallographic orientations. Energy Dispersive X-ray Spectroscopy (EDS) was performed using a UK Bruker XFlash 6130 EDS Detector (Thermo Fisher Scientific, Waltham, MA, USA) and Velox Analytical Software 3.15.0. A drop of the prepared particle suspensions was deposited onto copper TEM grids coated with an amorphous carbon lacy film, followed by drying prior to the S/TEM examination.

### 2.6. Scanning Electron Microscopy (SEM) and EDS

A Sirion 400NC (FEI, Hillsboro, OR, USA) with an INCA 350 EDS (Oxford Instruments, Abingdon, Oxfordshire, UK) was used for the SEM/EDS analyses. A droplet of the samples (Fe<sub>3</sub>O<sub>4</sub> and Fe<sub>3</sub>O<sub>4</sub>-Au suspensions) was set on an SEM stub holder with graphite tape and left to dry in a desiccator. The dried samples were then coated with carbon for increased conductivity during the SEM imaging and EDS analysis.

### 2.7. Dynamic Light Scattering (DLS) and Zeta Potential

DLS analysis and zeta potential measurements were used on a suspension of Fe<sub>3</sub>O<sub>4</sub> and Fe<sub>3</sub>O<sub>4</sub>-Au. The samples were moved into an omega cuvette and put into a DLS analysis machine. The analysis was conducted on a Malvern Zetasizer Nano ZS instrument (Malvern Panalytical, Worcestershire, UK). The statistical analysis was performed with the Excel program (Microsoft).

### 2.8. Magnetic Measurement

Room temperature magnetic hysteresis loops of dried samples (Fe<sub>3</sub>O<sub>4</sub> and Fe<sub>3</sub>O<sub>4</sub>-Au suspensions) were measured with a vibrating-sample magnetometer VSM Lake Shore 7307 (Lake Shore Cryotronics, Westerville, OH, USA).

### 3. Results

#### 3.1. XRD Analysis

Figure 2 represents the results of the XRD analysis of  $\text{Fe}_3\text{O}_4$  nanoparticles. The XRD analysis showed characteristic diffraction patterns typical of magnetite ( $\text{Fe}_3\text{O}_4$ ). The peaks at  $2\theta$  at 30.1, 35.5, 42.6, and 57.0, can be attributed to diffractions at the (220), (311), (400), and (511) planes, which are characteristic of magnetite [24].

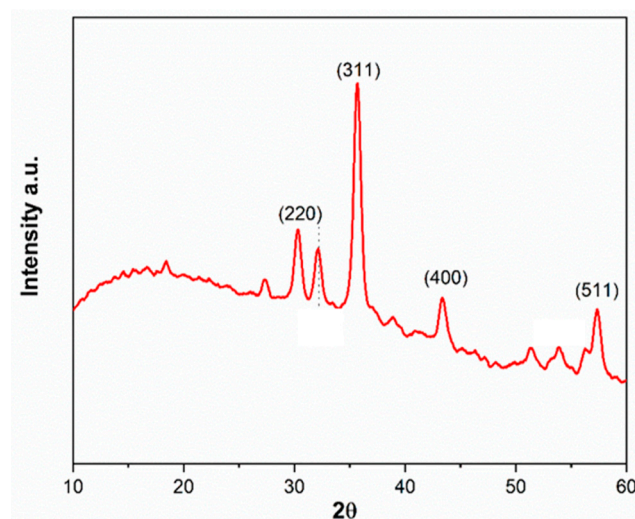


**Figure 2.** XRD analysis of  $\text{Fe}_3\text{O}_4$  nanoparticles.

#### 3.2. ICP-OES Results of the $\text{Fe}_3\text{O}_4$ and $\text{Fe}_3\text{O}_4$ -Au Suspensions

The measuring concentration of Fe in the prepared  $\text{Fe}_3\text{O}_4$  suspension is given in Table 1, while the resulting concentration of Fe and Au elements in the prepared  $\text{Fe}_3\text{O}_4$ -Au suspension is given in Table 2.

**Table 1.** ICP-OES result of Fe in the prepared  $\text{Fe}_3\text{O}_4$  suspension.

Sample	mg/mL Fe
$\text{Fe}_3\text{O}_4$	4.88

**Table 2.** ICP-OES analysis of Fe and Au in the prepared  $\text{Fe}_3\text{O}_4$ -Au hybrid nanostructures suspension.

Sample	$\mu\text{g/mL Fe}$	$\mu\text{g/mL Au}$
$\text{Fe}_3\text{O}_4$ -Au	7.0	40.6

#### 3.3. TEM Analysis

The TEM images of  $\text{Fe}_3\text{O}_4$  and  $\text{Fe}_3\text{O}_4$ -Au were analyzed to assess their morphology before and after USP. Figure 2 presents the TEM results for the  $\text{Fe}_3\text{O}_4$ . In Figure 3a,c, clusters of  $\text{Fe}_3\text{O}_4$  are observed, with some NPs exhibiting spherical shapes, while others are irregular. The particle sizes range from 5 nm to 25 nm, although significant aggregation is evident. The EDS analysis (Figure 3b) revealed a prominent oxygen peak, alongside two Fe-L and Fe-K peaks, indicating a high iron content in the sample. A small silicon peak was also detected, likely due to contamination, or originating from the substrate material. Figure 3d displays a 2-D Fast Fourier Transform (FFT), characterized by a concentric ring diffraction pattern with some brighter, more distinct spots. This suggests the presence of larger crystallites, while the continuity of the rings indicates that the crystallites are small (in the nanometer range) and oriented randomly, signifying a nanocrystalline material. Each ring corresponds to a specific set of crystallographic planes within the NPs. The ring pattern suggests that the NPs are crystalline, composed of numerous small crystallites with

varying orientations. The sharp, regularly spaced spots and rings suggest that the NPs are highly crystalline, with well-defined atomic planes. The presence of rings, rather than single diffraction spots, indicates that the NPs are not single crystals, but consist of multiple crystallites in random orientations. The electron diffraction pattern can be indexed to the  $\text{Fe}_3\text{O}_4$  cubic phase of iron oxide, as illustrated in Figure 3d.

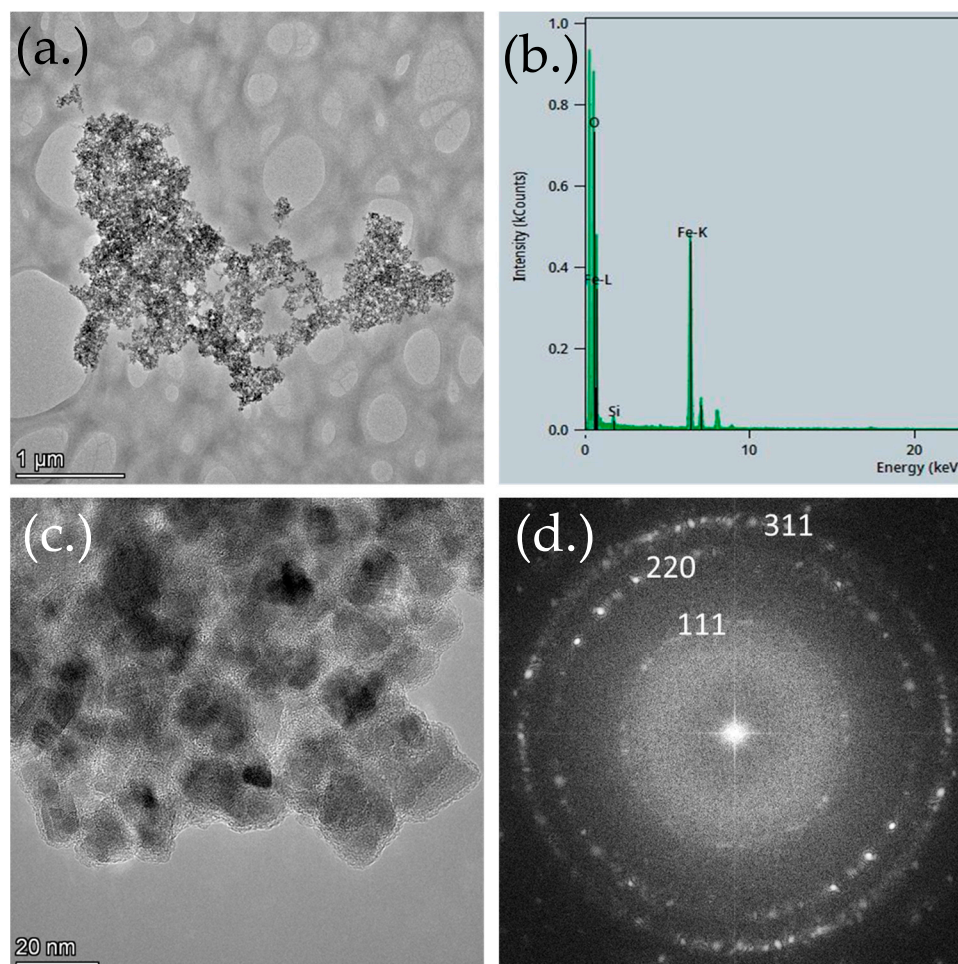


**Figure 3.** (a.) TEM bright-field (BF) image of the  $\text{Fe}_3\text{O}_4$  at lower magnification; (b.) EDS analysis of the  $\text{Fe}_3\text{O}_4$ ; (c.) TEM BF image of the  $\text{Fe}_3\text{O}_4$  at higher magnification; (d.) 2-D FFT image showing the concentric ring pattern of the  $\text{Fe}_3\text{O}_4$ .

Figure 4 shows the TEM and STEM results of  $\text{Fe}_3\text{O}_4$ -Au, with a lower magnification overview of the produced particles in Figure 4a and a higher magnification image of a typical  $\text{Fe}_3\text{O}_4$ -Au particle in Figure 4b. This section was examined additionally with EDS mapping and two selected area analyses in Figure 4c,d. The TEM images show clusters of smaller  $\text{Fe}_3\text{O}_4$ , covered with somewhat larger AuNPs with spherical and irregular shapes. The  $\text{Fe}_3\text{O}_4$  has similar sizes as without the Au, in a range from 5 nm to 25 nm. They also appear to be aggregated, as before. The AuNPs are larger, in a range of about 10 to 200 nm. The EDS mapping analysis shows a distribution of O, Fe, and Au, with the O and Fe seemingly overlapping. Additionally, C was detected but was removed from the analysis, as its presence is the result of the sample holder (TEM grid with lacy carbon film) and the stabilizer used for the particle collection during the USP process (PVP stabilizer). Some separate AuNPs were also present in the  $\text{Fe}_3\text{O}_4$ -Au sample. An example is shown in Figure 4e, showing a measured fringe spacing of 0.20 nm, which is in very good agreement with the cell parameters of Au and the particle oriented in the (200) direction, along with

an FFT pattern of this particle in Figure 4f. The spot pattern indicates a crystalline structure of the produced AuNPs, with indices as shown in Figure 4e.

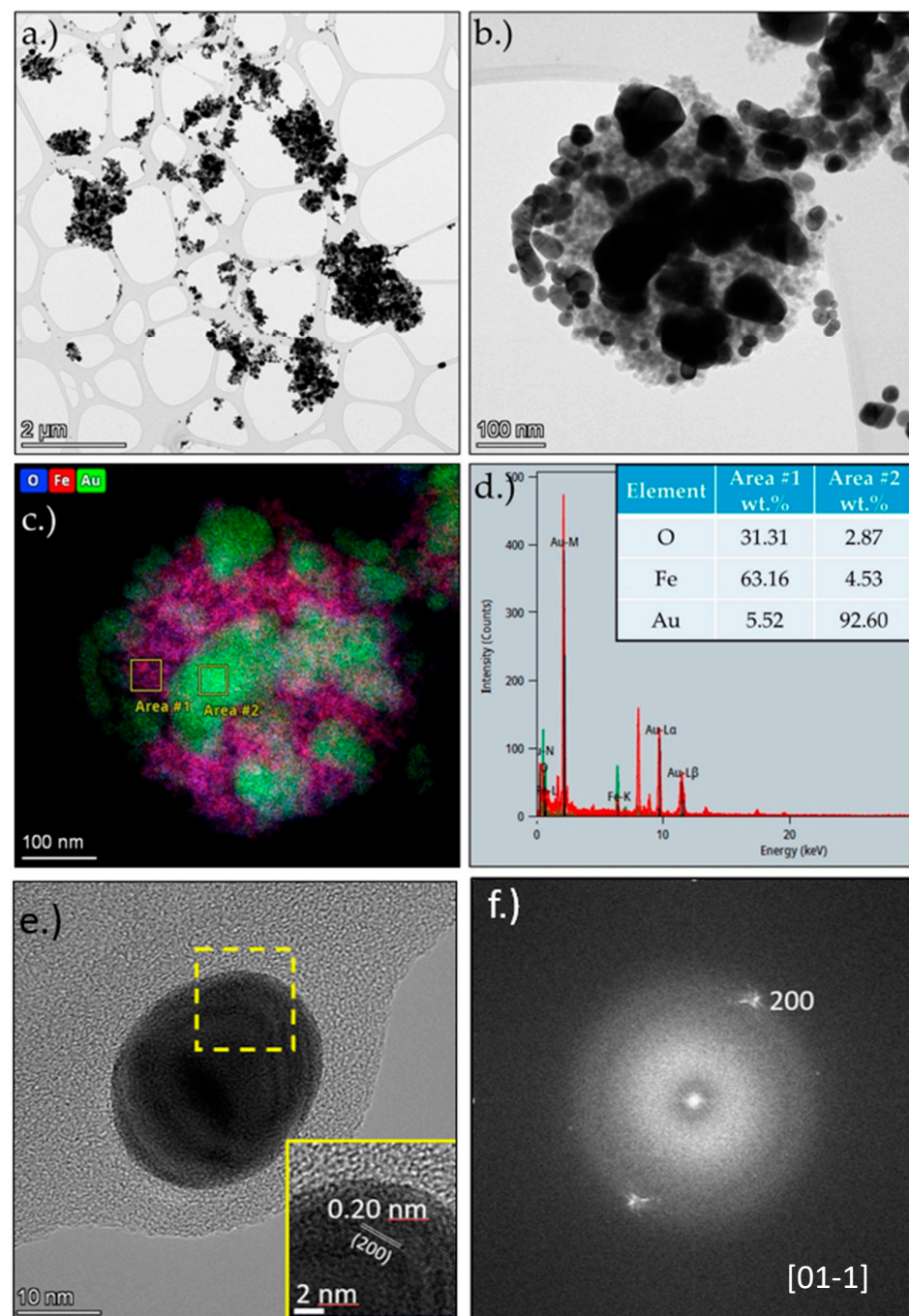


**Figure 4.** (a.) Lower magnification TEM bright-field (BF) overview image of  $\text{Fe}_3\text{O}_4$ -Au particles prepared by USP; (b.) Higher magnification STEM BF image of an example of the produced  $\text{Fe}_3\text{O}_4$ -Au; (c.) STEM/EDS mapping image of the  $\text{Fe}_3\text{O}_4$ -Au; (d.) STEM/EDS analysis of the marked areas of the  $\text{Fe}_3\text{O}_4$ -Au; (e.) Selected Au NPs with HR-TEM image of the selected area (included as the inset); (f.) 2-D FFT image showing the spots pattern of an AuNPs.

### 3.4. SEM Analysis

In Figure 5a, the suspension of  $\text{Fe}_3\text{O}_4$  in water is shown, where the settling of the NPs is clearly visible, in addition to some NPs floating. Figure 5b,c showcase the results of the SEM analysis. The particle size is between 20 and 40 nm, which corresponds to the results

of the TEM analysis. In the EDS analysis (Figure 5d) of the  $\text{Fe}_3\text{O}_4$ , carbon and oxygen can be observed with the addition of iron. The carbon was present because of the graphite tape used to prepare the samples. The oxygen and iron are the result of the  $\text{Fe}_3\text{O}_4$ .

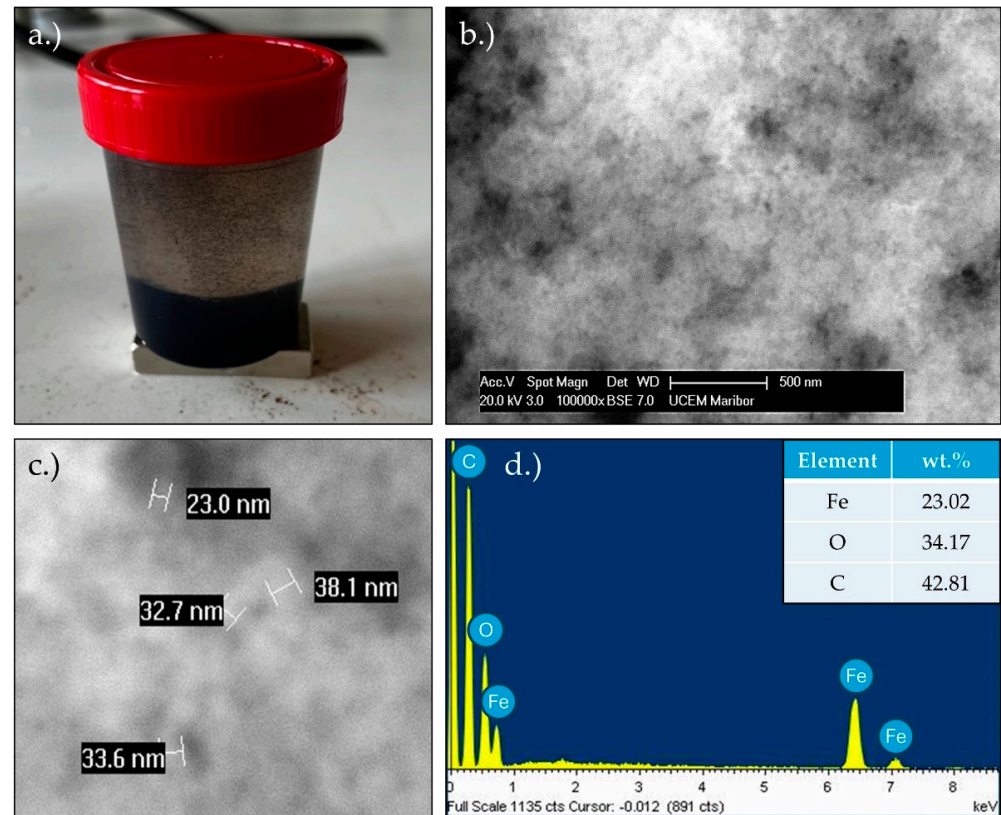


**Figure 5.** (a.) Suspension of the  $\text{Fe}_3\text{O}_4$  in water; (b.) SEM image of the  $\text{Fe}_3\text{O}_4$ ; (c.) SEM image of the  $\text{Fe}_3\text{O}_4$  with particle sizes measured; and (d.) EDS analysis of the  $\text{Fe}_3\text{O}_4$ .

Figure 6 shows the SEM/EDS analysis performed on  $\text{Fe}_3\text{O}_4$ -Au hybrid nanostructures. The particle structures are similar to the TEM images, wherein the  $\text{Fe}_3\text{O}_4$  clusters are covered with irregularly shaped AuNPs, along with some individual AuNPs present as separate entities. The EDS shows the presence of C, O, Cl, Fe, and Au. Again, the carbon is present due to the graphite tape on which the sample was deposited, as well as due to the stabilizer PVP. Chlorine is a side product of the USP process, which was additionally collected from the USP gas flow, along with the collection of the particles in the collection medium.

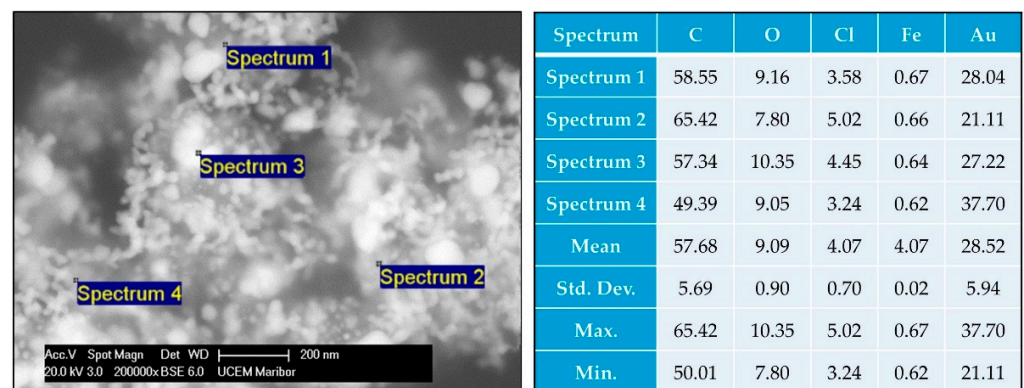


**Figure 6.** SEM image of the  $\text{Fe}_3\text{O}_4$ -Au hybrid nanostructures with EDS analysis of selected particles.

### 3.5. DLS and Zeta Potential Analysis

In Figure 7, we can see the graph of the DLS analysis of the  $\text{Fe}_3\text{O}_4$  NPs. The peak is located at values around 50–100 nm, with the average hydrodynamic diameter being around 65 nm, a polydispersity index of 36%, and a standard deviation of approximately 39 nm. A standard deviation of 39 nm means that, on average, the  $\text{Fe}_3\text{O}_4$  NPs sizes deviated by 39 nm from the average hydrodynamic diameter. D10 is approximately 15.08 nm and D90 is about 115 nm, which indicates that 10% of NPs are smaller than 15.08 nm, and 90% are smaller than 115 nm. The median value (D50) of the hydrodynamic diameter (62 nm) is close to the mean value (65 nm), indicating a symmetric distribution of  $\text{Fe}_3\text{O}_4$  NPs sizes. The presence of one peak indicates that the NPs are relatively monodisperse, meaning that they have a consistent size around this value. We can also observe no other peak that would indicate the presence of much larger NPs.

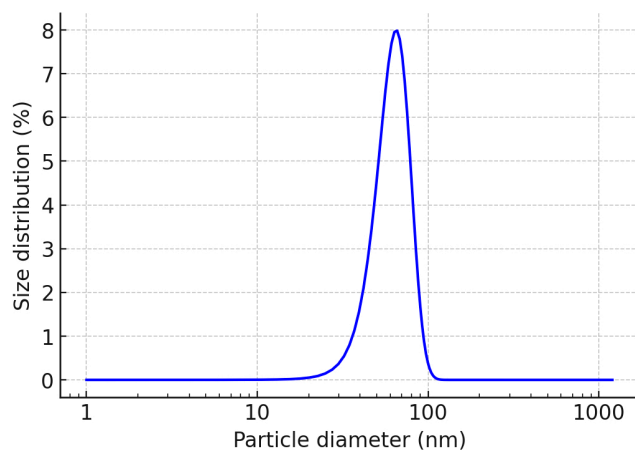


**Figure 7.** Dynamic light scattering analysis of  $\text{Fe}_3\text{O}_4$ .

In Figure 8, we can see the results of the DLS analysis of  $\text{Fe}_3\text{O}_4$ -Au hybrid nanostructure samples. The largest peak is located at values 200–300 nm, which suggests that most of the NPs have a diameter between 200 and 300 nm, with the average hydrodynamic diameter being 279 nm, polydispersity index of 33%, and a standard deviation of 160 nm. A standard deviation means that, on average, the  $\text{Fe}_3\text{O}_4$ -Au sizes deviated by 160 nm from the average hydrodynamic diameter. D10 is approximately 74 nm and D90 is about 483 nm, which indicates that 10% of the NPs are smaller than 74 nm, and 90% are smaller than 483 nm. The median value (D50) of the hydrodynamic diameter (255 nm) is close to the mean value (279 nm), indicating a symmetric distribution.

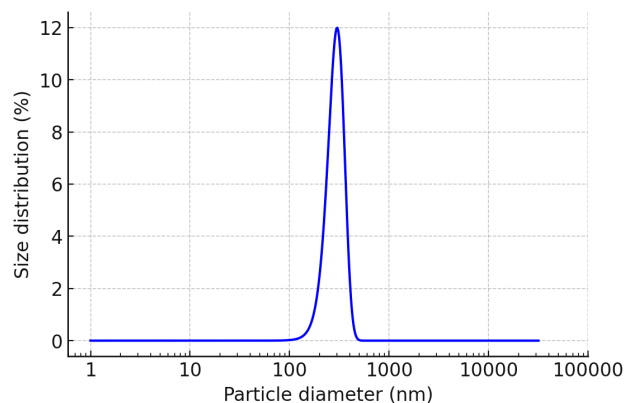


**Figure 8.** Dynamic light scattering analysis of  $\text{Fe}_3\text{O}_4$ -Au.

It is important to note that DLS measures the hydrodynamic diameter of NPs in suspension, which includes not only the core NP size but also any surface coatings and

solvent layers that contribute to the overall NP size in the medium. In the case of NPs with a non-uniform or incomplete gold coating, the DLS measurements may not reflect the true size of the core NPs accurately. This is because DLS measures the apparent hydrodynamic diameter, which could be influenced by the uneven distribution of the coating material, resulting in an overestimation of the total NPs size. Furthermore, the aggregation of NPs can also contribute to an increased measured hydrodynamic diameter. Non-contiguous coatings may alter the surface properties of the NPs, leading to variable interactions with the surrounding medium, and subsequently impacting the DLS results. As such, the DLS data should be interpreted with these potential contributions in mind, recognizing that the measured size could reflect both the aggregated state of the NPs and the uneven nature of the surface coating.

The discrepancy between the NP sizes measured using DLS and those measured via TEM or SEM is quite common. DLS measurements tend to show larger NP sizes for several reasons. DLS measures the hydrodynamic diameter, which includes not only the core of the NPs, but also any surface layers or adsorbed molecules (e.g., surfactants, polymers, or solvent molecules) surrounding the NPs. This hydrodynamic shell can make them appear larger than they are. In contrast, TEM and SEM provide the physical (core) diameter of the NPs, which does not account for these surrounding layers. In DLS, if NPs aggregate or form small clusters, the technique will report the size of these larger aggregates rather than individual particles. This can skew the results toward larger sizes. TEM and SEM typically measure individual NPs, as the drying process in sample preparation often breaks aggregates apart. Additionally, DLS is more sensitive to larger NPs or aggregates, because the scattering intensity scales with the sixth power of the NPs' radius, meaning large NPs affect the results disproportionately. In DLS, NPs are measured in a liquid medium, and their hydrodynamic size reflects interactions with the solvent. NPs in solution may absorb a hydration layer, increasing their apparent size. TEM and SEM are performed under vacuum or on dry samples, where such hydration layers are absent, leading to smaller size measurements. This explains why the DLS results are usually higher than those obtained via TEM or SEM analysis.

Figure 9 represents the zeta potential result of the  $\text{Fe}_3\text{O}_4$ . The peak is relatively sharp, which indicates that most particles have a similar surface charge. The values on the x-axis range from approximately  $-100$  mV to  $+100$  mV, with the peak centered close to  $-15$  mV. This suggests that most of the particles in the suspension have a zeta potential near neutral (close to  $0$  mV). It was concluded that the  $\text{Fe}_3\text{O}_4$  suspension is close to its isoelectric point (which is around pH 6.5–7 for  $\text{Fe}_3\text{O}_4$ ) [25,26], consequently, the electrostatic repulsion between the particles is minimal. This indicates that the NPs are less stable and prone to aggregation, as there is not enough repulsion to keep the particles apart.

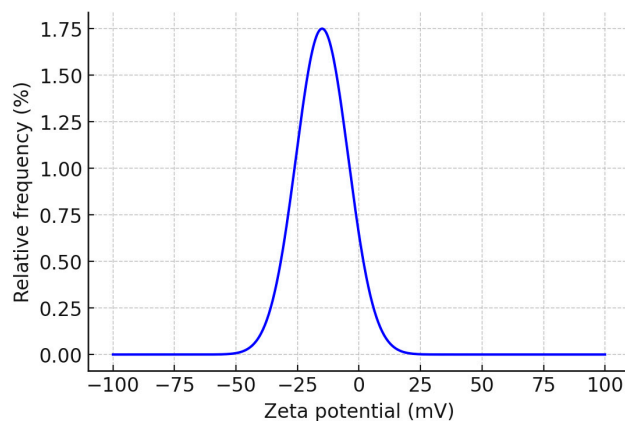


**Figure 9.** Zeta potential analysis of the  $\text{Fe}_3\text{O}_4$ .

Figure 10 represents the results of the zeta potential measurement of the  $\text{Fe}_3\text{O}_4$ -Au hybrid nanostructures. On the graph is a peak, with its center at around  $0$  mV with a

median zeta potential of  $-0.49$  mV. This suggests that the NPs exhibit a relatively neutral surface charge. The distribution of the zeta potential is very narrow, meaning that most of the particles have very similar surface charge properties, as reflected in the small variance around the peak. A low zeta potential (close to 0 mV) implies poor stability. The optimal zeta potential for stable suspensions is usually around  $-30$  mV or  $+30$  mV [27,28]. In the case of  $\text{Fe}_3\text{O}_4$ -Au hybrid nanostructures, the zeta potential being close to zero can be attributed to the surface chemistry and the nature of the AuNPs. Au is a noble metal, and its surface is relatively inert, which means it does not form strong ionic interactions easily in aqueous solutions. As a result, the AuNPs' presence on the  $\text{Fe}_3\text{O}_4$  surface, can, effectively, neutralize, or screen the surface charge of the underlying  $\text{Fe}_3\text{O}_4$  core, leading to a reduced overall surface charge. This can result in a near-neutral zeta potential.

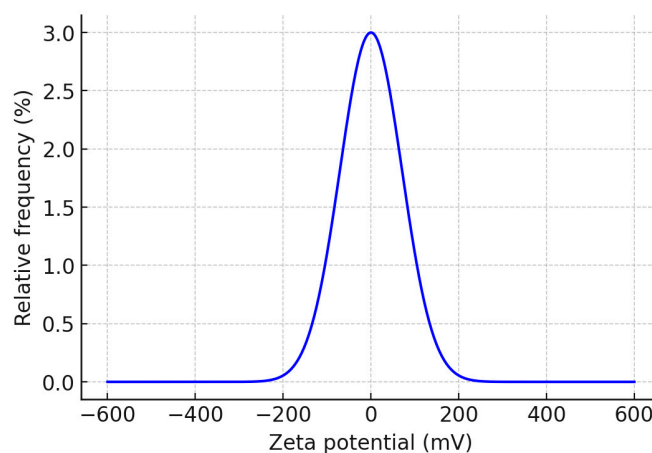


**Figure 10.** Zeta potential analysis of the  $\text{Fe}_3\text{O}_4$ -Au hybrid nanostructures.

### 3.6. Magnetic Properties

Figure 11a represents a magnetic hysteresis loop of  $\text{Fe}_3\text{O}_4$ , labeled “MNP<sub>s</sub>-1\_8”. The  $x$ -axis represents the external magnetic field  $H$  in Oersted’s (Oe), from  $-20,000$  to  $+20,000$  Oe. The  $y$ -axis represents the magnetization  $M$  in emu/g, which extends from  $-40$  emu/g to  $+40$  emu/g. The curve is strongly S-shaped and appears to saturate at both ends (around  $35$ – $40$  emu/g for large positive and negative fields). There is no visible coercivity or remanence (the point at which the loop crosses the  $x$ -axis is very close to zero), which implies that this material exhibits superparamagnetic behavior. The transition to the superparamagnetic state in magnetite NPs typically occurs for particles with diameters below  $25$  to  $30$  nm, as reported in the literature [29,30]. The exact critical size depends on factors such as the shape and surface modification of the NPs, but, in general, magnetite particles smaller than this threshold exhibit superparamagnetic behavior [29,30].

The saturation magnetization is determined from the point where the magnetization reaches a plateau, indicating that further increases in the applied magnetic field do not result in a significant increase in magnetization. Looking at Figure 11a, the magnetization appears to saturate around  $35$  emu/g, which is in the range of typical values ( $30$ – $50$  emu/g) reported for nanosized iron oxide particles [31,32]. The saturation magnetization of bulk magnetite at room temperature is generally reported to be in the range of  $92$  to  $100$  emu/g [29]. However, for magnetite NPs, the saturation magnetization is often lower than the bulk value and can vary depending on factors like particle size, shape, and surface properties. For instance, smaller magnetite NPs typically exhibit lower saturation magnetization values. Another reason for a decrease in saturation magnetization is because of the aggregation of NPs. NPs have a high surface-to-volume ratio, which leads to many surface atoms. These surface atoms often have disordered spins, due to broken bonds or surface oxidation. When NPs aggregate, the surface effects become more pronounced, because the interactions between surface spins are not as strong as the interactions in the bulk. This disordered spin state at the surface leads to a reduction in the overall magnetization [29,30].

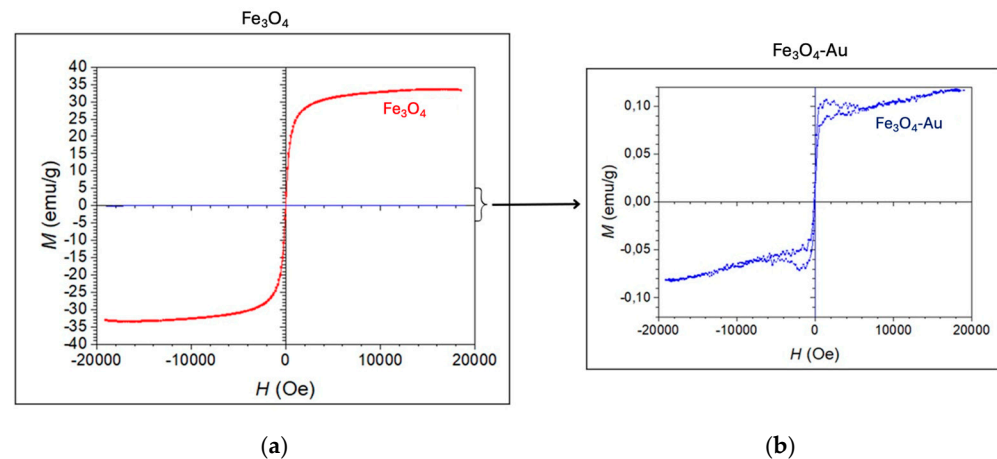


**Figure 11.** Magnetic hysteresis loop of (a)  $\text{Fe}_3\text{O}_4$  NPs and (b)  $\text{Fe}_3\text{O}_4$ -Au hybrid nanostructures.

Figure 11b represents a magnetic hysteresis loop of  $\text{Fe}_3\text{O}_4$ -Au hybrid nanostructures. The figure also shows a typical “S-shaped” curve, characteristic of superparamagnetic or weakly ferromagnetic materials. In this case, the loop has no significant coercivity (the field required to bring the magnetization to zero), and no remanent magnetization (residual magnetism when the external field is removed). This indicates that the material aligns quickly with and demagnetizes with the external field, suggesting superparamagnetic behavior. There is no significant hysteresis loop area, indicating very low or no coercivity and remanent magnetization. This implies the NPs are superparamagnetic at room temperature, meaning they only exhibit magnetism in the presence of an external field and lose their magnetization once the field is removed. The curve appears to saturate at around  $\pm 0.10$  emu/g for large magnetic fields (close to 20,000 Oe). This represents the maximum magnetization of the  $\text{Fe}_3\text{O}_4$ -Au hybrid nanostructures in the presence of a strong magnetic field, beyond which further increases in the magnetic field do not increase magnetization significantly. To calculate the volume fraction of magnetite ( $\text{Fe}_3\text{O}_4$ ) and gold in the  $\text{Fe}_3\text{O}_4$ -Au hybrid nanostructures we used the following equation:

$$f(\text{magnetite}) = \frac{M(\text{hybrid nanostructures})}{M(\text{magnetite})}$$

$$f(\text{magnetite}) = \frac{0.1 \text{ emu/g}}{35 \text{ emu/g}}$$

$$f(\text{magnetite}) = 0.0029 = 0.29\%$$

The volume fraction of gold is the remainder since the total volume must be equal to 1 or 100%

$$f(\text{gold}) = 1 - 0.0029 = 0.9971 = 99.71\%$$

Based on the results, we can see that the  $\text{Fe}_3\text{O}_4$ -Au hybrid nanostructures contain very little magnetic material—most of the sample was gold (99.71% by volume), and the rest was magnetite (0.29% by volume). In the analysis of the magnetization behavior, we recognize that it is challenging to observe the saturation magnetization clearly from the data presented. One potential factor contributing to this is the diamagnetic contribution of the presence of Au, which could affect the overall magnetization signal and lead to an apparent suppression of the saturation magnetization. Au is a diamagnetic material and can introduce a negative magnetic moment, which may reduce the net magnetization at higher fields and potentially mask the true saturation point of the magnetic NPs. This effect could result in an underestimation of the saturation magnetization and impact the accuracy of the analysis. Furthermore, measurements at higher magnetic fields would be beneficial to provide a clearer indication of the true saturation point. While the current data provide valuable insight into the general magnetic behavior of the coated NPs, future

studies should consider performing magnetization measurements at higher fields to ensure a more accurate determination of the saturation magnetization.

#### 4. Discussion

The Fe<sub>3</sub>O<sub>4</sub> NPs prepared with the coprecipitation method had spherical and some irregular shapes, within a size range of about 10 to 40 nm, and a highly crystalline structure. Aggregation was observed in the Fe<sub>3</sub>O<sub>4</sub> suspension, forming clusters of these NPs. The Fe<sub>3</sub>O<sub>4</sub> NPs exhibited superparamagnetic behavior. The different examinations showed that the Fe<sub>3</sub>O<sub>4</sub> retained their sizes, shapes, and aggregation properties. The Fe<sub>3</sub>O<sub>4</sub>-Au hybrid nanostructures had weaker magnetization but still had superparamagnetic behavior, owing to the presence of Fe<sub>3</sub>O<sub>4</sub>, as Au does not have this property.

The resulting Fe<sub>3</sub>O<sub>4</sub>-Au hybrid nanostructures were not uniform, with Fe<sub>3</sub>O<sub>4</sub> clusters covered with spherical and irregular AuNPs. Individual separate AuNPs were observed in the synthesized suspension after USP. During the USP process, the formation of AuNPs was bimodal, as AuNPs were formed on the surface of the Fe<sub>3</sub>O<sub>4</sub>, as well as directly from the dried Au-chloride droplets, into AuNPs. The bimodal formation of AuNPs observed in the study—where AuNPs were deposited both on Fe<sub>3</sub>O<sub>4</sub> surfaces and as separate entities—has been a recurring challenge in hybrid nanostructure synthesis. Previous studies [29] have shown that aggregation during synthesis often leads to uneven coatings and variable nanoparticle sizes, which aligns with our findings. Furthermore, Moraes Silva et al. discussed similar difficulties when using alternative chemical reduction methods, highlighting the importance of controlling precursor ratios and preventing aggregation for uniform Au coatings [16].

Earlier research [29,30] on the USP production of Fe NPs coated with Au was performed using dissolved Fe-salts (Fe acetate, nitrate, and chloride) and Au salts in the precursor solution. The results showed that the Fe NPs forms depended greatly on the precursor used, forming meshes, and spherical or irregular structures of Fe-oxide NPs. The AuNPs were deposited on the Fe-oxide NPs with varying degrees of coverage, sizes, and shapes, depending on the process parameters and salt concentrations in the precursor solution. A full core-shell Fe-Au structure was not achieved in these investigations, and similar structures were formed as with the present investigation. The broad miscibility gap between Fe and Au resulted in complete phase separation between these two elements during the NPs' synthesis.

In the present investigation, already prepared Fe<sub>3</sub>O<sub>4</sub> NPs were used as seeds in the USP precursor solution for the achievement of Au coating on Fe<sub>3</sub>O<sub>4</sub> NPs. Depending on the coprecipitation method, Fe<sub>3</sub>O<sub>4</sub> with 1/8th of the chosen mass of iron sulfates was determined as the most appropriate for further processing with USP. These Fe<sub>3</sub>O<sub>4</sub> had the least aggregation and smallest sizes, making them the most suitable for use with the ultrasonic membrane. The sizes of the Fe<sub>3</sub>O<sub>4</sub> seeds are required to be as small as possible for generating aerosol droplets and transporting these droplets into the USP tube furnace. With large particle sizes in the precursor, the generated droplets do not contain these particles, as they are left behind in the precursor solution. The Fe<sub>3</sub>O<sub>4</sub> clusters should also be avoided in the precursor solution to provide for aerosol droplets containing the seeds for Au coating. The different characterizations showed a higher AuNP content as compared to Fe, with a larger mass quantity of Au present, as confirmed by ICP-OES. There was 5.8× more AuNP mass present than Fe<sub>3</sub>O<sub>4</sub> in the final Fe<sub>3</sub>O<sub>4</sub>-Au suspension. The initial concentration ratio for Fe and Au in the precursor solution was 4× more Au than Fe. This indicates that some Fe<sub>3</sub>O<sub>4</sub> may have been left behind in the precursor solution during droplet generation. Additional optimization of the Au-precursor solution containing Fe<sub>3</sub>O<sub>4</sub> is needed to improve the uptake of these particles in the aerosol droplets, such as further reduction of the particle sizes and prevention of particle cluster formations.

The characteristics of the Fe<sub>3</sub>O<sub>4</sub>-Au hybrid nanostructures are like previous experiments to produce core-shell Fe-Au NPs with one main difference. Previously, solid Fe NPs were obtained, covered with Au particles [29,30]. However, with this research, we

have obtained Fe<sub>3</sub>O<sub>4</sub> clusters, covered with AuNPs. Magnetic nanoparticles, such as Fe<sub>3</sub>O<sub>4</sub>, have a natural tendency to aggregate due to magnetic dipole–dipole interactions and van der Waals forces. This aggregation can potentially influence subsequent coating processes, such as USP, by affecting the overall surface area and the uniformity of the applied coating. In the USP coating process, particle aggregation could reduce the exposed surface area, potentially leading to uneven or patchy gold deposition. This may result in a non-uniform hybrid structure, as aggregation particles may only be coated on the outer surface of the cluster, leaving interior surfaces exposed. To mitigate these issues, dispersing agents, surfactants, or optimized sonication techniques, can help reduce aggregation before or during the coating process. Similar aggregation challenges have been reported, where they suggest the use of dispersing agents or surface stabilizers to enhance nanoparticle stability and coating uniformity [13]. Adopting such strategies could improve the homogeneity of Fe<sub>3</sub>O<sub>4</sub>-Au hybrid nanostructures prepared via USP.

To produce more uniformly covered Fe<sub>3</sub>O<sub>4</sub>, their surface needs to be adjusted for more favorable growth of Au during the USP process. The presence of chlorine in some of the analyses also indicates an unoptimized USP process, wherein some unreacted Au-salts may also be present in the final collection medium (water and stabilizer). These initial investigations of using Fe<sub>3</sub>O<sub>4</sub> seeds have given further insight and possible directions into investigating the possibilities of producing Fe<sub>3</sub>O<sub>4</sub>-Au hybrid nanostructures with USP.

The magnetic properties of the Fe<sub>3</sub>O<sub>4</sub> were retained in the final Fe<sub>3</sub>O<sub>4</sub>-Au hybrid nanostructures, although, the magnetization was diminished by the AuNPs content. By overcoming the issues with ultrasonic droplet generation with more optimal Fe<sub>3</sub>O<sub>4</sub> sizes in the precursor solution, and better Au coverage on the Fe<sub>3</sub>O<sub>4</sub>, the magnetic properties may be preserved further for better performance. The magnetic measurements revealed that saturation magnetization of Fe<sub>3</sub>O<sub>4</sub>-Au hybrid nanostructures was significantly reduced compared to Fe<sub>3</sub>O<sub>4</sub>. This can be attributed to surface effects, where disordered spins and the presence of a non-magnetic Au layer weaken the net magnetization. Similar reductions in magnetization for small Fe<sub>3</sub>O<sub>4</sub> nanoparticles due to surface spin effects have been documented, emphasizing the critical impact of nanoparticle size and aggregation on magnetic properties [32].

Additional optimization steps are needed for the determination of the parameters for the synthesis of Fe<sub>3</sub>O<sub>4</sub>-Au NPs (optimization of the Au/Fe<sub>3</sub>O<sub>4</sub> precursor for USP, surface modification of the Fe<sub>3</sub>O<sub>4</sub>). Studies have shown that fine control over precursor composition and droplet size is essential for achieving desired core-shell structures [23].

Currently, there are no specific studies that detail the synthesis of Fe<sub>3</sub>O<sub>4</sub> nanoparticles via the coprecipitation method followed by Au coating using USP. The coupling of coprecipitation and USP in this study provides a novel approach to synthesizing Fe<sub>3</sub>O<sub>4</sub>-Au hybrid nanostructures. Compared to chemical reduction and seed-mediated methods discussed by Moraes Silva et al. [16], USP offers distinct advantages in scalability but requires further optimization to address challenges such as bimodal Au formation and reduced Fe<sub>3</sub>O<sub>4</sub> incorporation. The results provide a valuable foundation for further exploration and optimization of Fe<sub>3</sub>O<sub>4</sub>-Au hybrid nanostructures with coprecipitation and USP.

## 5. Conclusions

The following conclusions emerged from this research:

Using the coprecipitation method it was possible to synthesize Fe<sub>3</sub>O<sub>4</sub> NPs successfully. The Fe<sub>3</sub>O<sub>4</sub> NPs exhibited superparamagnetic behavior, with sizes ranging from 5 nm to 25 nm, although significant aggregation was evident.

The process of coating the Fe<sub>3</sub>O<sub>4</sub> NPs with Au via USP resulted in the formation of separate AuNPs and Fe<sub>3</sub>O<sub>4</sub>-Au hybrid nanostructures. AuNPs were formed on the surface of individual Fe<sub>3</sub>O<sub>4</sub> NPs and their aggregates.

The resulting Fe<sub>3</sub>O<sub>4</sub>-Au hybrid nanostructures exhibited a range of sizes and structures, retaining the superparamagnetic behavior, while demonstrating a reduction in magnetization due to the added Au content. Separately formed AuNPs presented a crystalline

structure with sizes ranging from 10 to 200 nm, with one possible growth direction of AuNPs being [01-1].

**Author Contributions:** Conceptualization, R.R. and L.K.; methodology, L.K., K.P.Č. and R.R.; software, P.M.; validation, K.P.Č. and R.R.; formal analysis, L.K. and D.F.; investigation, L.K., K.P.Č., P.M. and R.R.; resources, K.P.Č. and R.R.; data curation, P.M.; writing—original draft preparation, L.K. and P.M.; writing—review and editing, P.M., D.F. and R.R.; visualization, L.K. and P.M.; supervision, R.R.; project administration, R.R.; funding acquisition, R.R. All authors have read and agreed to the published version of the manuscript.

**Funding:** This research and APC was funded by the Slovenian Research Agency ARIS (P2-0120 and P2-0118 Research Programs).

**Data Availability Statement:** The raw data supporting the conclusions of this article will be made available by the authors on request.

**Acknowledgments:** We would like to thank Žiga Jelen for his administrative assistance.

**Conflicts of Interest:** Authors Peter Majerič, Rebeka Rudolf were employed by the company Zlatarna Celje d.o.o. The remaining authors declare that the research was conducted in the absence of any commercial or financial relationships that could be construed as a potential conflict of interest.

### Abbreviations

AuNPs—gold nanoparticles, DLS—dynamic light scattering, EDS—dispersive X-ray spectroscopy, Fe<sub>3</sub>O<sub>4</sub>—magnetite, Fe<sub>3</sub>O<sub>4</sub>-Au—hybrid nanostructures, ICP-OES—optical emission spectrometry with inductively coupled plasma, NPs—nanoparticles, SEM—scanning electron microscopy, TEM—transmission electron microscopy, USP—ultrasonic spray pyrolysis, XRD—X-ray diffraction.

### References

1. Stiufiuc, G.F.; Stiufiuc, R.I.; Nanoparticles, M. Characterization, and Their Use in Biomedical Field. *Appl. Sci.* **2024**, *14*, 1623. [[CrossRef](#)]
2. Ali, A.; Shah, T.; Ullah, R.; Zhou, P.; Guo, M.; Ovais, M.; Tan, Z.; Rui, Y.K. Review on Recent Progress in Magnetic Nanoparticles: Synthesis, Characterization, and Diverse Applications. *Front. Chem.* **2021**, *9*, 629054. [[CrossRef](#)]
3. Shasha, C.; Krishnan, K.M. Nonequilibrium Dynamics of Magnetic Nanoparticles with Applications in Biomedicine. *Adv. Mater.* **2021**, *33*, 1904131. [[CrossRef](#)]
4. Stueber, D.D.; Villanova, J.; Aponte, I.; Xiao, Z.; Colvin, V.L. Magnetic nanoparticles in biology and medicine: Past, present, and future trends. *Pharmaceutics* **2021**, *13*, 943. [[CrossRef](#)] [[PubMed](#)]
5. Soetaert, F.; Korangath, P.; Serantes, D.; Fiering, S.; Ivkov, R. Cancer therapy with iron oxide nanoparticles: Agents of thermal and immune therapies. *Adv. Drug Deliv. Rev.* **2020**, *163*, 65–83. [[CrossRef](#)]
6. Luo, K.; Zhao, J.; Jia, C.; Chen, Y.; Zhang, Z.; Zhang, J.; Huang, M.; Wang, S.; Fe, I.O. Integration of Fe<sub>3</sub>O<sub>4</sub> with Bi<sub>2</sub>S<sub>3</sub> for Multi-Modality Tumor Theranostics. *ACS Appl. Mater. Interfaces* **2020**, *12*, 22650–22660. [[CrossRef](#)] [[PubMed](#)]
7. Gobbo, O.L.; Sjaastad, K.; Radomski, M.W.; Volkov, Y.; Prina-Mello, A. Magnetic nanoparticles in cancer theranostics. *Theranostics* **2015**, *5*, 1249–1263. [[CrossRef](#)]
8. Belyanina, I.; Kolovskaya, O.; Zamay, S.; Gargaun, A.; Zamay, T.; Kichkailo, A. Targeted magnetic nanotheranostics of cancer. *Molecules* **2017**, *22*, 975. [[CrossRef](#)]
9. Chang, D.; Lim, M.; Goos, J.A.C.M.; Qiao, R.; Ng, Y.Y.; Mansfeld, F.M.; Jackson, M.; Davis, T.P.; Kavallaris, M. Biologically targeted magnetic hyperthermia: Potential and limitations. *Front. Pharmacol.* **2018**, *9*, 831. [[CrossRef](#)]
10. Xie, J.; Liu, G.; Eden, H.S.; Ai, H.; Chen, X. Surface-engineered magnetic nanoparticle platforms for cancer imaging and therapy. *Acc. Chem. Res.* **2011**, *44*, 883–892. [[CrossRef](#)]
11. Rocha-Santos, T.A.P. Sensors and biosensors based on magnetic nanoparticles. *TrAC—Trends Anal. Chem.* **2014**, *62*, 28–36. [[CrossRef](#)]
12. Gupta, A.K.; Gupta, M. Synthesis and surface engineering of iron oxide nanoparticles for biomedical applications. *Biomaterials* **2005**, *26*, 3995–4021. [[CrossRef](#)] [[PubMed](#)]
13. De Souza, K.C.; Andrade, G.F.; Vasconcelos, I.; De Oliveira Viana, I.M.; Fernandes, C.; De Sousa, E.M.B. Magnetic solid-phase extraction based on mesoporous silica-coated magnetic nanoparticles for analysis of oral antidiabetic drugs in human plasma. *Mater. Sci. Eng. C* **2014**, *40*, 275–280. [[CrossRef](#)]
14. Gooding, J.J.; Ciampi, S. The molecular level modification of surfaces: From self-assembled monolayers to complex molecular assemblies. *Chem. Soc. Rev.* **2011**, *40*, 2704–2718. [[CrossRef](#)]

15. Yang, D.; Pang, X.; He, Y.; Wang, Y.; Chen, G.; Wang, W.; Lin, Z. Precisely Size-Tunable Magnetic/Plasmonic Core/Shell Nanoparticles with Controlled Optical Properties. *Angew. Chem.* **2015**, *127*, 12259–12264. [[CrossRef](#)]
16. Silva, S.M.; Tavallaie, R.; Sandiford, L.; Tilley, R.D.; Gooding, J.J. Gold coated magnetic nanoparticles: From preparation to surface modification for analytical and biomedical applications. *Chem. Commun.* **2016**, *52*, 7528–7540. [[CrossRef](#)]
17. Goon, I.Y.; Lai, L.M.H.; Lim, M.; Munroe, P.; Gooding, J.J.; Amal, R. Fabrication and dispersion of gold-shell-protected magnetite nanoparticles: Systematic control using polyethyleneimine. *Chem. Mater.* **2009**, *21*, 673–681. [[CrossRef](#)]
18. Cui, Y.R.; Hong, C.; Zhou, Y.L.; Li, Y.; Gao, X.M.; Zhang, X.X. Synthesis of orientedly bioconjugated core/shell Fe<sub>3</sub>O<sub>4</sub>@Au magnetic nanoparticles for cell separation. *Talanta* **2011**, *85*, 1246–1252. [[CrossRef](#)]
19. Ahmadi, A.; Shirazi, H.; Pourbagher, N.; Akbarzadeh, A.; Omidfar, K. An electrochemical immunosensor for digoxin using core-shell gold coated magnetic nanoparticles as labels. *Mol. Biol. Rep.* **2014**, *41*, 1659–1668. [[CrossRef](#)]
20. Kayal, S.; Ramanujan, R.V. Anti-cancer drug loaded iron-gold core-shell nanoparticles (Fe@Au) for magnetic drug targeting. *J. Nanosci. Nanotechnol.* **2010**, *10*, 5527–5539. [[CrossRef](#)]
21. Kumagai, M.; Sarmat, T.K.; Cabral, H.; Kaida, S.; Sekino, M.; Herlambang, N.; Osada, K.; Kano, M.R.; Nishiyama, N.; Kataoka, K. Enhanced in vivo magnetic resonance imaging of tumors by PEGylated iron-oxide-gold core-shell nanoparticles with prolonged blood circulation properties. *Macromol. Rapid Commun.* **2010**, *31*, 1521–1528. [[CrossRef](#)] [[PubMed](#)]
22. Salehizadeh, H.; Hekmatian, E.; Sadeghi, M.; Kennedy, K. Synthesis and characterization of core-shell Fe<sub>3</sub>O<sub>4</sub>-gold-chitosan nanostructure. *J. Nanobiotechnol.* **2012**, *10*, 3. [[CrossRef](#)] [[PubMed](#)]
23. Carpenter, E.E.; Sangregono, C.; O’connor, C.J. Effects of Shell Thickness on Blocking Temperature of Nanocomposites of Metal Particles with Gold Shell. *IEEE Trans. Magnetics* **1999**, *35*, 3496–3498. [[CrossRef](#)]
24. Shukla, S.; Jadaun, A.; Arora, V.; Sinha, R.K.; Biyani, N.; Jain, V.K. In vitro toxicity assessment of chitosan oligosaccharide coated iron oxide nanoparticles. *Toxicol. Rep.* **2015**, *2*, 27–39. [[CrossRef](#)]
25. Boucher, C.; Rubel, O.; Zhitomirsky, I. Supercapacitor Performance of Magnetite Nanoparticles Enhanced by a Catecholate Dispersant: Experiment and Theory. *Molecules* **2023**, *28*, 1562. [[CrossRef](#)] [[PubMed](#)]
26. Liu, M.; Ye, Y.; Ye, J.; Gao, T.; Wang, D.; Chen, G.; Song, Z. Recent Advances of Magnetite (Fe<sub>3</sub>O<sub>4</sub>)-Based Magnetic Materials in Catalytic Applications. *Magnetochemistry* **2023**, *9*, 110. [[CrossRef](#)]
27. Dai, X.; Dai, Y.; Zheng, Y.; Lv, Y. Magnetic nanoparticles and possible synergies with cold atmospheric plasma for cancer treatment. *RSC Adv.* **2024**, *14*, 29039–29051. [[CrossRef](#)]
28. Karpinska, K.; Li, L.; Wang, T. Dual conjugation of magnetic nanoparticles with antibodies and siRNA for cell-specific gene silencing in vascular cells. *Front. Drug Deliv.* **2024**, *4*, 1416737. [[CrossRef](#)]
29. Nguyen, M.D.; Tran, H.V.; Xu, S.; Lee, T.R. Fe<sub>3</sub>O<sub>4</sub> nanoparticles: Structures, synthesis, magnetic properties, surface functionalization, and emerging applications. *Appl. Sci.* **2021**, *11*, 11301. [[CrossRef](#)]
30. Kemp, S.J.; Ferguson, R.M.; Khandhar, A.P.; Krishnan, K.M. Monodisperse magnetite nanoparticles with nearly ideal saturation magnetization. *RSC Adv.* **2016**, *6*, 77452–77464. [[CrossRef](#)]
31. Balakrishnan, T.; Lee, M.J.; Dey, J.; Choi, S.M. Sub-nanometer scale size-control of iron oxide nanoparticles with drying time of iron oleate. *CrystEngComm* **2019**, *21*, 4063–4071. [[CrossRef](#)]
32. Nedelkoski, Z.; Kepaptsoglou, D.; Lari, L.; Wen, T.; Booth, R.A.; Oberdick, S.D.; Galindo, P.L.; Ramasse, Q.M.; Evans, R.F.L.; Majetich, S.; et al. Origin of reduced magnetization and domain formation in small magnetite nanoparticles. *Sci. Rep.* **2017**, *7*, 45997. [[CrossRef](#)] [[PubMed](#)]

**Disclaimer/Publisher’s Note:** The statements, opinions and data contained in all publications are solely those of the individual author(s) and contributor(s) and not of MDPI and/or the editor(s). MDPI and/or the editor(s) disclaim responsibility for any injury to people or property resulting from any ideas, methods, instructions or products referred to in the content.